Electrowetting-based beam scanner with controllable field of view

Rui Zhao[1,*], Kai Zhang[1], Songfeng Kou[2,3], Xian Wei[1], Zhongcheng Liang[1]

[1]Center of Optofluidic Technology, College of Optoelectronic Engineering,
 Nanjing University of Posts and Telecommunications,
 Nanjing 210023, China

[2]National Astronomical Observatories/Nanjing Institute of Astronomical Optics & Technology,
 Chinese Academy of Sciences, Nanjing 210042, China

[3]CAS Key Laboratory of Astronomical Optics & Technology,
 Nanjing Institute of Astronomical Optics & Technology,
 Nanjing 210042, China

*Corresponding author: zhaor@njupt.edu.cn

A beam scanner based on electrowetting with controllable field of view is designed. Depending on the first-order paraxial approximation, the scanning path and scanning radius of the beam scanner are derived. Its physical model and properties are established and analyzed with the help of by using the COMSOL and MATLAB. The results show that the scanning beam emitting from the beam scanner realizes 360° scanning freely, and its controllable field of view varies from 0 to 65.3 m successfully under the action of working voltage. The two liquid interfaces in the beam scanner can rotate clockwise or counterclockwise independently, and their inclination angle ranges from 0° to 45°. When the two liquid interfaces turn in the same direction, the scanning effect of edge field is better than that of the central zone. While the scanning effect of the central area is greatly improved and better than that of the edge field when the two liquid interfaces turn in the different direction. In addition, the rotation frequencies of the two interfaces affect the performance of the beam scanner.

Keywords: beam scanner, electrowetting, controllable field of view, COMSOL, MATLAB.

1. Introduction

Beam scanning technology has been widely used in laser communications, medical detection, thermal imaging and other fields [1-3]. The universal joint and scanning galvanometer system such as Risley prisms and MEMS mirror are employed to achieve beam scanning in traditional mechanical beam scanners [4-6]. However, the beam scanners mentioned above have the problems of large size, complex structures, large mechanical inertia and poor scanning accuracy limiting the application of beam scan-

ners. More importantly, their scanning radius cannot be changed once the structure of the traditional beam scanner is determined. Therefore, a non-mechanical beam scanner with controllable field of view, simple structure, easy miniaturization and high modulation precision is desirable.

Since electrowetting has the advantages of non-mechanical operation, fast response speed, and no electromagnetic interference, electrowetting-based beam scanners have been proposed recently [7,8]. In 2016, Kopp *et al.* designed an electrowetting driven optofluidic system as a two-dimensional laser scanner, whose inclination angle of the liquid interface varies from $-6.4°$ to $6.4°$, and the liquid interface can be rotated $360°$ [9]. In 2018, Supekar *et al.* integrated a liquid prism into a traditional two-photon microscope for beam scanning, which can provide a scanning range of $\pm 2°$ at 950 nm wavelength, and the scanning speed can reach $21°$/sec [10]. In 2020, Lim *et al.* has demonstrated a method for electrowetting-based beam scanner to improve mean positional accuracy [11].

In this paper, an electrowetting-based beam scanner with controllable field of view is designed. The operating mechanism and scanning performance are simulated by COMSOL and MATLAB. The results show that our proposed system achieves $360°$ rotation scanning freely, and its controllable scanning radius can vary from 0 to 65.3 m successfully under the action of working voltage. The system will promote the development of Laser Radar and has a wide range of applications.

2. Structure design and working principle

The electrowetting-based beam scanner shown in Fig. 1(a) is filled with two different liquids, whose cavity is designed as a hexadecagonal cylinder. In the cavity, the top and bottom liquid are both conductive liquid (1 wt% SDS deionized liquid, refractive index $n_1 = 1.33$), while the middle liquid is insulating liquid (mixed liquid of 5 wt% dodecane and 1-chloro-naphthalene, refractive index $n_2 = 1.617$), whose correspond-
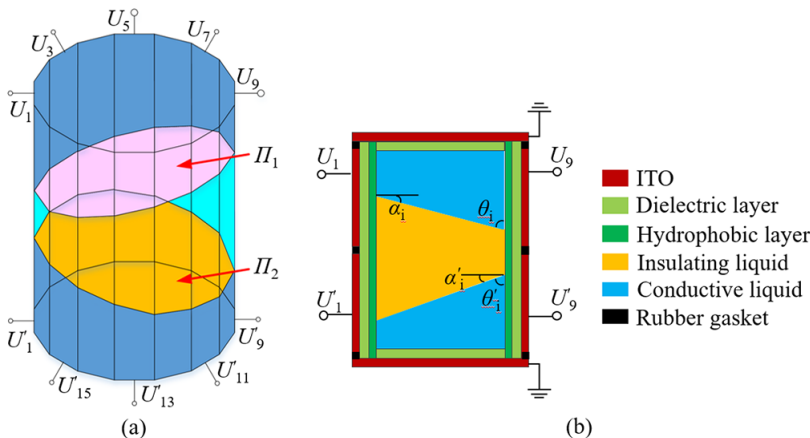

Fig. 1. Schematic diagram of electrowetting-based beam scanner.

ing height is 2.5, 5, and 2.5 mm, respectively. The sidewall of the beam scanner is divided into upper and lower parts by ITO electrode separation. The inner surface of the cavity is coated with dielectric layer and a hydrophobic layer shown in Fig. 1(b).

The working voltages U_i and U_i' are applied on the sidewall of cavity, where U_i and U_{i+8}, U_i' and U_{i+8}' are pairs of electrodes, $i = 1, 2...8$ [12]. The inclination angles of two liquid planar interfaces α_1 and α_1' are determined by contact angle θ_i shown in Fig. 1(b), where θ_i is calculated by the Young–Lippmann equation listed below [13]:

$$\cos \theta_i = \cos \theta_0 + \frac{1}{2} \frac{\varepsilon}{d\,\gamma} U_i^2 \tag{1}$$

$$\alpha_1 = \alpha_1' = \frac{\pi}{2} - \theta_1 \tag{2}$$

here U_i is the working voltage, θ_0 is the initial contact angle, ε and d is the electric permittivity and the thickness of dielectric layer, and γ is the liquid surface tension, respectively.

When proper different voltages are applied on electrode pairs (U_i and U_{i+8}, U_i' and U_{i+1}'), the contact angle θ_i at electrodes U_i can be expressed as [9]

$$\theta_i = \frac{\pi}{2} - \left(\frac{\pi}{2} - \theta_1\right) \cos\left[\frac{\pi}{8}(i-1)\right], \qquad 1 \le i \le 8 \tag{3}$$

where θ_1 is contact angle on electrode U_1. Once the contact angle θ_i is known, the voltage U_i can be calculated by Eq. (1). By varying the voltages, the inclination angles of liquid planar interfaces α_1 and α_1' change, and then corresponding liquid interfaces with certain inclination angles rotates clockwise or counterclockwise independently [14].

Figure 2(a) shows the scanning principle of the electrowetting-based beam scanner. For convenience, the hexadecagonal cylinder is simplified as a circular cavity for theoretical analysis. When the incident beam S enters into the beam scanner along the optical axis, it passes through the lower cover sheet Π_0, the lower liquid interface Π_1,
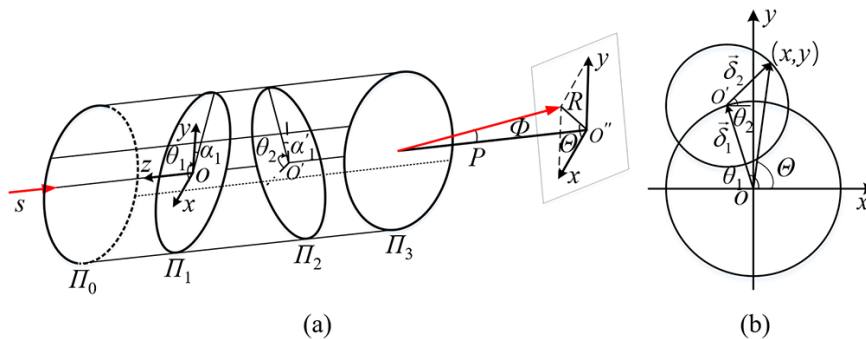

Fig. 2. Scanning principle of electrowetting-based beam scanner. (a) Schematic diagram of beam scanner, and (b) first-order paraxial approximation methods for rotating scanning of liquid interfaces Π_1 and Π_2.

the upper liquid interface Π_2, and the upper cover sheet Π_3. The inclination angles of the liquid interfaces Π_1 and Π_2 are α_1 and α'_1, and its rotation angles are θ_1 and θ_2, respectively. Generally, the scanning distance P is large enough to ignore the beam displacement inside the beam scanner. Φ denotes the altitude angle of the outgoing beam, the azimuth angle Θ is the included angle of the outgoing beam with the x axis, *i.e.*, the polar angle in polar coordinate system, and the polar radius R refers to the distance from the center point O'' to the receiving point.

As mentioned above, the liquid interfaces Π_1 and Π_2 in Fig. 2 can rotate around z axis clockwise or counterclockwise independently by controlling the sidewall electrodes. The altitude angle Φ and the azimuth angle Θ will change with the rotation of the interfaces Π_1 and Π_2. Consequently, once the inclination angles α_1 and α'_1 of the interfaces Π_1 and Π_2 are changed, the beam scanning field of view and the corresponding scanning radius will be variable.

The first-order paraxial approximation method is employed to depict the rotation of the liquid interfaces Π_1 and Π_2 shown in Fig. 2(b). When the interface Π_1 rotates, the deviation vector $\boldsymbol{\delta}_1$ rotates around point O and its relative rotation angle is θ_1, where $\boldsymbol{\delta}_1$ represents the deviation vector of incident beam after passing through the liquid interface Π_1. Similarly, the deviation vector $\boldsymbol{\delta}_2$ will rotate around point O' and its corresponding rotation angle is θ_2 when the interface Π_2 rotates, here $\boldsymbol{\delta}_2$ represents the deviation vector of the incident beam passing through the liquid interface Π_2.

The total deviation of the two liquid interfaces (Π_1, Π_2) equals the vector sum of $\boldsymbol{\delta}_1$ and $\boldsymbol{\delta}_2$. The projection components of the total ray deviation on X and Y axes can be written as:

$$\delta_X = \delta_1 \cos\theta_1 + \delta_2 \cos\theta_2 \tag{4a}$$

$$\delta_Y = \delta_1 \sin\theta_1 + \delta_2 \sin\theta_2 \tag{4b}$$

The rotation angles θ_1 and θ_2 for interfaces Π_1 and Π_2 are:

$$\theta_1 = 2\pi f_1 t + \varphi_{10} \tag{5a}$$

$$\theta_2 = \pm 2\pi f_2 t + \varphi_{20} \tag{5b}$$

here f_1 and f_2 represent the rotation frequency of Π_1 and Π_2, respectively; φ_{10} and φ_{20} represent the initial rotation angle of Π_1 and Π_2. When Π_2 rotates counterclockwise, θ_2 is assumed to be positive; while it is negative when Π_2 rotates clockwise.

Substituting Eq. (5) into Eq. (4), we can get:

$$\delta_X = \delta_1 \cos(2\pi f_1 t + \varphi_{10}) + \delta_2 \cos(\pm 2\pi f_2 t + \varphi_{20}) \tag{6a}$$

$$\delta_Y = \delta_1 \sin(2\pi f_1 t + \varphi_{10}) + \delta_2 \sin(\pm 2\pi f_2 t + \varphi_{20}) \tag{6b}$$

Define the scanning period T of the beam scanner as the least common multiple of the rotation period of Π_1 and Π_2.

$$T = nT_1 = mT_2 \tag{7}$$

here $T_1 = 1/f_1$, and $T_2 = 1/f_2$; T_1 and T_2 refer the rotation period of Π_1 and Π_2, respectively; n and m are prime numbers.

The ratio of rotation frequency f_1 and f_2 of the interfaces Π_1 and Π_2 is defined as K

$$K = \frac{m}{n} = \frac{T_1}{T_2} = \frac{f_2}{f_1} \tag{8}$$

The polar radius R' and polar angle Θ are used to depict the spot of scanning beam, which can be expressed as follow:

$$R' = P(\delta_1 + \delta_2) \left| \cos\left[\frac{\pi(f_1 \mp f_2)t}{2} + \frac{\varphi_{10} - \varphi_{20}}{2} \right] \right| \tag{9}$$

$$\Theta = \pi(f_1 \pm f_2)t + \frac{\varphi_{10} - \varphi_{20}}{2} \tag{10}$$

here (R', Θ) is the position of final scanning point in polar coordinates. It can be calculated by geometric knowledge and Snell's law:

$$R = P \tan\left\{ \sin^{-1}\left[\frac{n_1}{n_0} \sin\left(\tan^{-1} \frac{R'}{P} \right) \right] \right\} \tag{11}$$

According to Eq. (9), the maximum scanning radius can be written as follows:

$$R'_{\max} = P(\delta_1 + \delta_2) \tag{12}$$

Substituting Eq. (12) into Eq. (11), the maximum scanning radius $R_{\max}$ is written as

$$R_{\max} = P \tan\left\{ \sin^{-1}\left[\frac{n_1}{n_0} \sin\left(\tan^{-1}\left((\alpha_1 + \alpha_1')(n_2 - n_1) \right) \right) \right] \right\} \tag{13}$$

Equation (13) indicates that the scanning radius R of the beam scanner is only determined by the inclination angle α_1 and α_1' since the scanning distance P and the refractive index of the liquids remain unchanged. Therefore, in theory, the scanning radius of the beam scanner can be adjusted continuously with the variation of the inclination angles within a certain range under the action of the working voltage.

3. Simulation and analysis

3.1. Inclination and rotation of interfaces Π_1 and Π_2

The electrowetting-based beam scanner is established in COMSOL, and the relative parameters are provided in Table 1. In this work, 1 wt% SDS deionized liquid is used

T a b l e 1. Parameters of beam scanner.

Parameter	Value	Definition
D	5 mm	Bottom width
H	10 mm	Height
$\theta 0$	160°	Zero voltage contact angle
γ	0.0075 N/m	Surface tension
ε	2.65	Relative dielectric constant
H_{diel}	1 µm	Dielectric thickness

as conductive liquid, while 5 wt% dodecane and 1-CN (1-chloro-naphthalene) mixed liquid acts as the insulating liquid.

Figure 3 shows the inclination angles α_1 and α_1' of the two liquid interfaces $\varPi_1$ and $\varPi_2$ at different working voltages. Sixteen pairs of electrodes are fixed on the
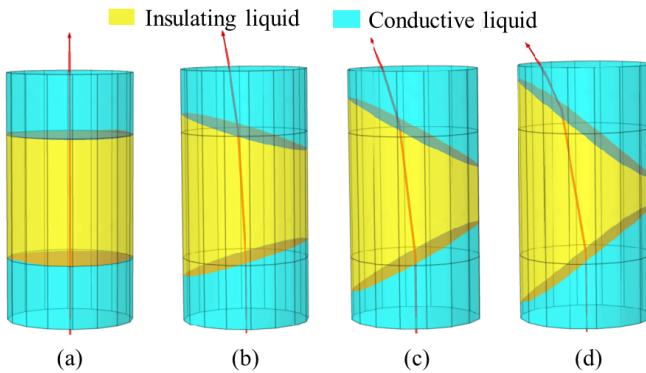

Fig. 3. Variation of inclination angles (α_1, α_1') at different working voltages: (a) $U_1 = 24.5$ V, $\alpha_1 = \alpha_1' = 0°$, (b) $U_1 = 21$ V, $\alpha_1 = \alpha_1' = 15°$, (c) $U_1 = 16.9$ V, $\alpha_1 = \alpha_1' = 30°$, (d) $U_1 = 12.2$ V, $\alpha_1 = \alpha_1' = 45°$.
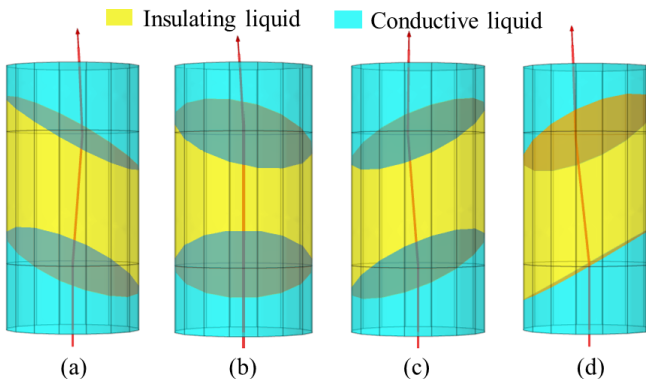

Fig. 4. Rotation of liquid interface $\varPi_1$ and $\varPi_2$ at different rotation angles θ_1 and θ_2: (a) $\theta_2 = -22.5°$, $U_1 = 17.5$ V; $\theta_1 = 45°$, $U_1' = 29.0$ V, (b) $\theta_2 = -67.5°$, $U_1 = 21.9$ V; $\theta_1 = 90°$, $U_1' = 24.5$ V, (c) $\theta_2 = -135°$, $U_1 = 29$ V; $\theta_1 = 135°$, $U_1' = 19.4$ V, (d) $\theta_2 = -215°$, $U_1 = 29$ V; $\theta_1 = 180°$, $U_1' = 16.9$ V.

hexadecagonal cylinder. For simplicity, only the working voltage U_1 on electrode 1 is mentioned in Fig. 3. The inclination angles (α_1, α_1') increase with the decrease of the working voltage. Due to the electrowetting saturation, the inclination angle α_1 and α_1' varies from 160° to 45° independently under action of specific voltage combination [15]. It is easily to find that the corresponding scanning field of view increases with the inclination angles (α_1, α_1').

Set the inclination angles (α_1, α_1') as fixed value 30°, and rotate the two interfaces (Π_1, Π_2) clockwise or counterclockwise. From Fig. 4, it is easy to find that the altitude angle Φ and azimuth angle Θ shown in Fig. 2 will change once the two interfaces (Π_1, Π_2) are rotated or the rotation angels (θ_1, θ_2) are variable.

3.2. Scanning method of beam scanner

In this section, the following parameters are assigned to fixed values, *i.e.*, the inclination angle $\alpha_1 = \alpha_1' = 40°$, the scanning distance $P = 100$ m. The rotation frequency f_1 remains 20 r/min, while the rotation frequency f_2 is chosen as 1, 13, and 19 r/min, respectively. So, the relative rotation frequency ratio $K (= f_2 : f_1)$ equals 0.1, 0.65, and 0.95.

When the interfaces Π_1 and Π_2 rotate along the same direction at different frequency ratio $K (= f_2 : f_1)$, the scanning path is spiral circles shown in Fig. 5. It shows that the number of spiral circles decreases gradually when the ratio of the rotation frequency K increases. The decrease of spiral circles means that the repetitive scanning rate is reduced, which means that the corresponding blind area is reduced and the relative scanning quality is improved. Consequently, the edge of the field of view without blind scanning zone can be realized once the rotation frequency ratio K closes to 1. Of course, the scanning quality in the center is better than that of the edge when the rotation frequency ratio K is small.

When the interfaces Π_1 and Π_2 rotate in different direction at different frequency ratios, the scanning path is changed, which is shown in Fig. 6. Similarly, the rotation
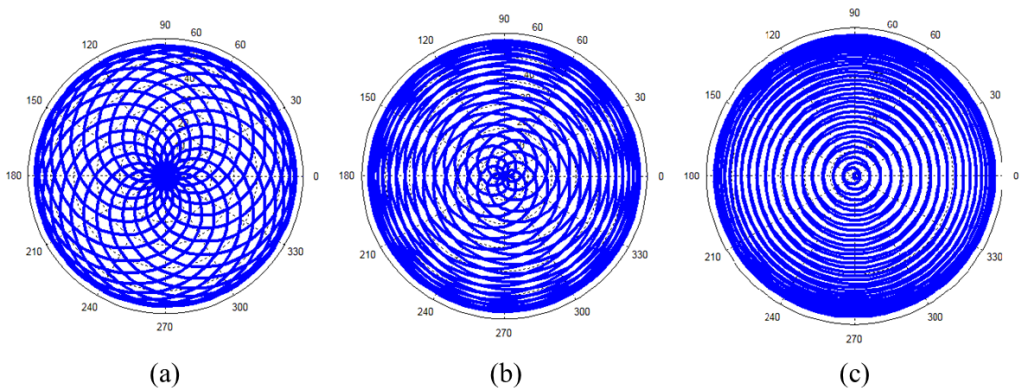

(a)   (b)   (c)
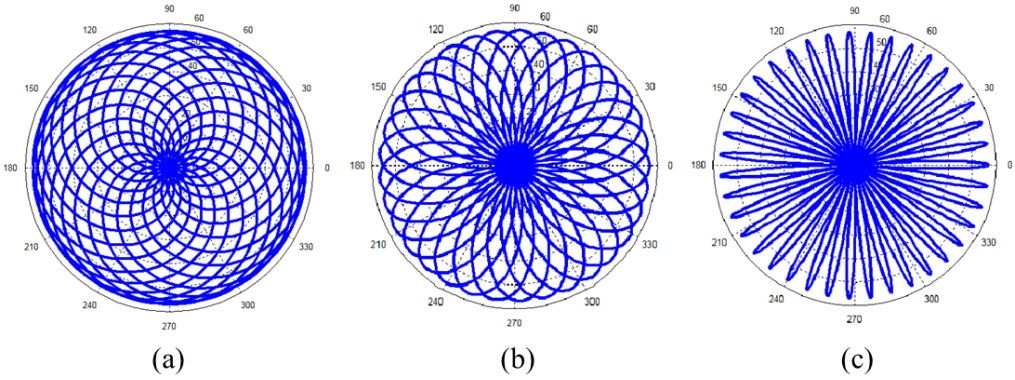
Fig. 5. The scanning path of the liquid interfaces rotating in the same direction at different frequency ratios, $f_1 = 20$ r/min, $\alpha_1 = \alpha_2 = 40°$ (a) $f_2 = 1$ r/min, $K = 0.05$, (b) $f_2 = 13$ r/min, $K = 0.65$, (c) $f_2 = 19$ r/min, $K = 0.95$.

Fig. 6. The scanning path of the liquid interfaces rotating in the opposite direction at different frequency ratios, $f_1 = 20$ r/min, $\alpha_1 = \alpha_2 = 40°$ (a) $f_2 = 1$ r/min, $K = 0.05$, (b) $f_2 = 13$ r/min, $K = 0.65$, (c) $f_2 = 19$ r/min, $K = 0.95$.

frequencies affect scanning performance of the beam scanner shown in Fig. 5. Compared with Fig. 5, the relative parameters remain unchanged except for the rotation directions of Π_1 and Π_2 interfaces. It can be seen from that the scanning performance and scanning area in the center field of view increase gradually with rotation frequency ratio K. By comparing Fig. 5 with Fig. 6, to realize no blind scanning in the whole area, the interfaces Π_1 and Π_2 can rotate in different direction and then in the same direction at high frequency ratio.

3.3. Scanning radius of beam scanner

Figure 7 shows the change of beam scanning radius at different inclination angles with the interfaces Π_1 and Π_2 rotating along the same direction. When the inclination angles α_1 and α_1' are assigned the same values 15°, 30° and 45°, the corresponding scanning radius are 20.2, 41.4, and 65.3 m, respectively. It can be concluded that the inclination
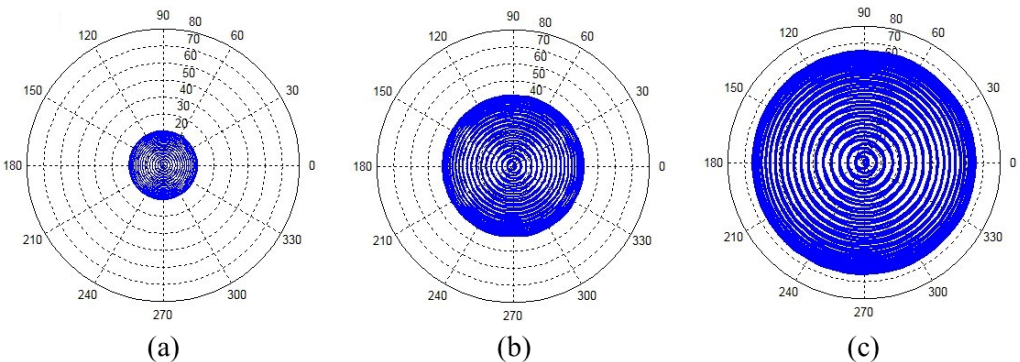

Fig. 7. Beam scanning radius at different inclination angles (α_1, α_2) when interfaces Π_1 and Π_2 rotates in the same direction ($f_1 = 20$ r/min, $f_2 = 19$ r/min) (a) $\alpha_1 = \alpha_2 = 15°$, (b) $\alpha_1 = \alpha_2 = 30°$, (c) $\alpha_1 = \alpha_2 = 45°$.
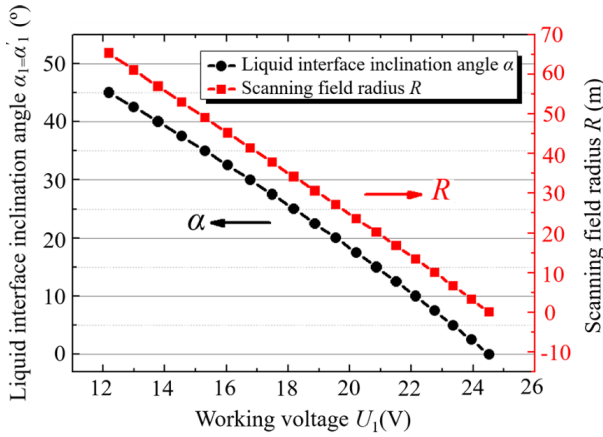
Fig. 8. Variation of inclination angle and scanning field radius *vs.* voltage.

angle of interfaces Π_1 and Π_2 affects the scanning radius directly. The scanning radius increases with inclination angles (α_1, α_1'). In other words, the scanning radius can be adaptively modulated to achieve an optimal beam scanning quality in different applications.

Figure 8 provides the variation of inclination angle (α_1, α_1') and scanning radius R under the action of working voltage, where the black dotted line (●) describes the inclination angle while the red square (■) dotted line depicts the scanning radius. When the working voltage is increased from 12.2 V to 24.5 V, the inclination angle (α_1, α_1') of liquid interfaces decrease from 45° to 0°. Meanwhile, the scanning radius varies from 65.3 to 0 m with the increasing voltage. The corresponding datatable of our beam scanner are provided in Table 2.

T a b l e 2. The corresponding datatable of beam scanner.

No.	Inclination angle	Scanning radius [m]	Scanning angle [deg]
1	0	0	0
2	15	20.2	11.4
3	30	41.4	22.5
4	45	65.3	33.1

4. Conclusion

The electrowetting-based beam scanner with controllable scanning radius is proposed in this work. COMSOL and MATLAB are used to simulate the inclination and rotation of the interfaces Π_1 and Π_2, the scanning mode and the scanning radius of the beam scanner. And a theoretical model is constructed to verify the simulation of the scanning radius and scanning path. The results show that the inclination angle varies from 0° to 45° and the associated scanning radius of our beam scanner ranges from 0 to 65.3 m

when the voltage ranges from 12.2 to 24.5 V. In addition, the two liquid interfaces Π_1 and Π_2 can independently rotate in either a clockwise or counterclockwise direction. To realize the scanning performance without blind zone, the interfaces Π_1 and Π_2 need to be rotated firstly in different direction and then in same direction. Wide range of applications of this electrowetting-based beam scanner can be expected.

References

[1] ZHANG H., YUAN Y., SU L., HUANG F., *Beam steering uncertainty analysis for Risley prisms based on Monte Carlo simulation*, Optical Engineering **56**(1), 2017: 014105. https://doi.org/10.1117/1.OE.56.1.014105

[2] LI J., CHEN K., PENG Q., WANG Z., JIANG Y., FU C., REN G., *Improvement of pointing accuracy for Risley prisms by parameter identification*, Applied Optics **56**(26), 2017: 7358-7366. https://doi.org/10.1364/AO.56.007358

[3] SONG D., CHANG J., ZHAO Y., ZHAO Q., *Risley prisms scanning optical imaging system using liquid crystal spatial light modulator*, Current Optics and Photonics **3**(3), 2019: 215-219. https://doi.org/10.3807/COPP.2019.3.3.215

[4] KUMAR K., AVRITSCHER R., WANG Y., LANE N., MADOFF D.C., YU T.K., YU T.-K., ZHANG X., *Handheld histology-equivalent sectioning laser-scanning confocal optical microscope for interventional imaging*, Biomedical Microdevices **12**(2), 2010: 223-233. https://doi.org/10.1007/S10544-009-9377-6

[5] LAI S.F., LEE C.C., *Double-wedge prism scanner for application in thermal imaging systems*, Applied Optics **57**(22), 2018: 6290-6299. https://doi.org/10.1364/AO.57.006290

[6] LI A., LI Q., DENG Z., ZHANG Y., *Risley-prism-based visual tracing method for robot guidance*, Journal of the Optical Society of America A **37**(4), 2020: 705-713. https://doi.org/10.1364/JOSAA.381445

[7] CLEMENT C.E., THIO S.K., PARK S.Y., *An optofluidic tunable Fresnel lens for spatial focal control based on electrowetting-on-dielectric (EWOD)*, Sensors and Actuators B: Chemical **240**, 2017: 909-915. https://doi.org/10.1016/J.SNB.2016.08.125

[8] LIU C., WANG D., WANG Q.H., XING Y., *Multifunctional optofluidic lens with beam steering*, Optics Express **28**(5), 2020: 7734-7745. https://doi.org/10.1364/OE.388810

[9] KOPP D., LEHMANN L., ZAPPE H., *Optofluidic laser scanner based on a rotating liquid prism*, Applied Optics **55**(9), 2016: 2136-2142. https://doi.org/10.1364/AO.55.002136

[10] SUPEKAR O.D., OZBAY B.N., ZOHRABI M., NYSTROM P.D., FUTIA G.L., RESTREPO D., GIBSON E.A., GOPINATH J.T., BRIGHT V.M., *Two-photon laser scanning microscopy with electrowetting-based prism scanning*, Biomedical Optics Express **8**(12), 2017: 5412-5426. https://doi.org/10.1364/BOE.8.005412

[11] LIM W.Y., ZOHRABI M., GOPINATH J.T., BRIGHT V.M., *Calibration and characteristics of an electrowetting laser scanner*, IEEE Sensors Journal **20**(7), 2019: 3496-3503. https://doi.org/10.1109/JSEN.2019.2959792

[12] CHENG J., CHEN C.L., *Adaptive beam tracking and steering via electrowetting-controlled liquid prism*, Applied Physics Letters **99**(19), 2011: 191108. https://doi.org/10.1063/1.3660578

[13] Smith N.R., Abeysinghe D.C., Haus J.W., Heikenfeld J., *Agile wide-angle beam steering with electrowetting microprisms*, Optics Express **14**(14), 2006: 6557-6563. https://doi.org/10.1364/OE.14.006557

[14] Horng J.S., Li Y., *Error sources and their impact on the performance of dual-wedge beam steering systems*, Applied Optics **51**(18), 2012: 4168-4175. https://doi.org/10.1364/AO.51.004168

[15] Zhang W.J., Zhao R., Kong M.M., Chen T., Guan J.F., Liang Z.C., *Simulation of beam steering control in arrayed liquid prisms system based on electrowetting-on-dielectric*, Optoelectronics Letters **16**(5), 2020: 321-326. https://doi.org/10.1007/S11801-020-9167-1